The Role of Noble and Base Metal Speciation and Surface Segregation in Ni_{2-x}Rh_xP Nanocrystals on Electrocatalytic Water Splitting Reactions in Alkaline Media

Tharanga N. Batugedara¹ and Stephanie L. Brock^{1,*}

¹Department of Chemistry

Wayne State University, Detroit, MI 48202 USA

*Email: sbrock@chem.wayne.edu

ABSTRACT

Transition metal phosphides have proven to be surprisingly active electrocatalysts for electrochemical water splitting, but the nature of the "active" catalyst depends strongly on the solution pH, the identity of the metals, and whether the reactions are anodic (oxygen evolution reaction, OER) or cathodic (hydrogen evolution reaction, HER). In order to understand the origin of this activity, the synthesis of well-defined, compositionally controlled pre-catalysts is needed, as are detailed catalytic studies and physicochemical characterization/activity assessment of catalysts at different stages. While base metal phosphides of Ni and Co have the advantage of being earth abundant, in alkaline media they are less active and less stable than noble metal phosphides such as Rh₂P. As a means to combine the abundant nature of base metals with the activity and stability of noble metals, the first synthesis of colloidal Ni_{2-x}Rh_xP nanocrystals by arrested precipitation routes is reported along with their composition-dependent activity for electrocatalytic HER and OER. Phase-pure samples of Ni_{2-x}Rh_xP were realized at the Ni-rich (hexagonal, Fe₂P-type) end (x = 0.00, 0.25, 0.50) and Rh-rich (cubic, antifluorite-type) end (x = 0.00, 0.25, 0.50) 1.75, 2.00). When assessed in terms of current density normalized to electrochemical surface area (ECSA) at fixed potential, the most active pre-catalyst for OER is Ni_{1.75}Rh_{0.25}P and for HER it is Rh_{1.75}Ni_{0.25}P. Evaluation of X-ray photoelectron spectroscopy, transmission electron microscopy/energy dispersive spectroscopy and ECSA data before and after 10 h stability runs were performed. The data reveal surface compositions to be considerably richer in Ni and poorer in Rh and P relative to the bulk composition, particularly for Ni_{0.25}Rh_{1.75}P where the surface ratio of Ni:Rh is nearly 2:1, and increases to 4:1 after HER catalysis. In all cases, surface phosphorus is completely depleted post-catalysis, suggesting a sacrificial role for phosphide under alkaline conditions. Moreover, the activity of "Rh_{1.75}Ni_{0.25}P" for HER decreases over time, even as the ECSA continues to rise, attributed to a decrease in the more active and stable Rh sites relative to Ni on the surface. In contrast, the enhancement in OER activity of Ni₂P with 12.5% Rh incorporation is attributed to restructuring upon phase-segregation of Rh, suggesting that the noble metal may also play a sacrificial role and not directly participate in OER catalysis. The roles of minority noble metals (Rh) in base-metal phosphides for OER and of minority base metals in noble-metal (Rh) phosphides for HER are discussed in light of related data on Co_{2-x}Rh_xP.

INTRODUCTION

Modern energy management is a balancing act between efforts to preserve natural resources, mitigate climate change, and satisfy increasing demands for inexpensive power. Renewable energy from the sun, wind, or tides has the potential to address these challenges, but is non-continuous, requiring a mechanism to "store" the energy for uninterrupted supply of power. Hydrogen (H₂) is poised to play a key role in energy management because of its high energy density, the ability to store this energy indefinitely without losses (in contrast to batteries and supercapacitors), and its clean combustion (water is the only byproduct). Electrochemical water splitting, when driven by renewable energy sources, provides a mechanism for generation of highly pure hydrogen, which can be used to produce electrical energy "on-demand" by the use of fuel cells.

The water electrolysis process consists of two half-cell reactions: the hydrogen evolution reaction (HER), which occurs at the cathode, and the oxygen evolution reaction (OER), which occurs at the anode. While the HER process produces the fuel (hydrogen) it is the OER process, which is responsible for generating the electrons and protons used to form hydrogen at the cathode, that is the slow step, so optimization of both processes is critical for efficient water splitting. The mechanism of HER and OER is highly pH-dependent, and as HER is facilitated by a high concentration of protons, the focus on electrocatalytic HER has largely been on the use of acidic media (pH = 0). However, the kinetically-limiting OER step is more favored in base (pH = 14), providing a strong motivation for the development of modern alkaline electrolyzers.^{1, 2} A major limiting factor in the widespread adoption of water electrolysis is the absence of inexpensive, highly efficient catalysts for HER and OER that are stable under these extreme pH conditions. This need provides a driving force for the discovery of new catalytic materials, and transition metal phosphides have emerged as a promising class of materials in this regard.

Phosphides were suggested as suitable catalysts for HER by Rodriguez and co-workers in 2005 based on DFT calculations conducted on Ni₂P that revealed a moderation in bonding of intermediates and products on the (001) plane due the combination of Lewis acidity of the Ni (acting as a hydride acceptor) and Lewis basicity of the phosphide (acting as a proton-acceptor) associated with the ensemble effect (the separation of Ni sites by P).³ The activity of Ni₂P was validated experimentally by Schaak and Lewis in 2013, where Ni₂P was found to exhibit a low-overpotential and high-stability (in acid) relative to other earth-abundant catalysts investigated.⁴ This spurred widespread investigation of transition metal phosphides for first HER, and subsequently OER, and related reactions.⁵⁻¹¹

While very good HER catalysts in acid and alkali, base metal phosphides do not outperform noble metals, prompting the study of noble metal phosphides. Work done by Duan *et al.* showed that Rh₂P nanocubes could be an excellent catalyst for HER, outperforming the activity and stability of Pt and Rh metals in acidic media. Likewise, Yang *et al* reported quasi spherical Rh₂P nanoparticles (~3 nm in sizes) to be the first Pt-free electrocatalyst that has a higher pH-universal HER performance compared to the state-of-the-art commercial Pt/C. With respect to OER, base metal phosphides are excellent pre-catalysts for OER in alkaline media (where they transform to

oxide/hydroxides), but are typically not stable at positive potentials in acid. $^{14, 15}$ In contrast, Rh_2P is an active catalyst for OER in acidic conditions, exhibiting a lower overpotential and enhanced stability relative to Pt/C; the overall stability is improved in alkaline media without sacrificing activity, such that Rh_2P can serve as a bifunctional catalyst for overall water electrolysis generating 200 mA/cm^2 for 1.7 V applied. 16

As a means to further limit the noble metal content, we sought to determine whether Rh₂P-type HER activity could be retained upon substitution of some of the noble metal content with base metals. Intriguingly, for Rh_{2-x}Co_xP nanocrystals, there was actually an enhancement of activity upon introduction of Co, and more significantly, replacement of up to 40% of Rh produced materials with activities comparable to Rh₂P in both acid and base. The catalysts demonstrated good stability in base, although Co was observed to leach under acidic conditions leading to a decrease and leveling off of activity in this system over time. Likewise, we found that Co₂P, a good base metal catalyst for OER in alkaline media, actually demonstrated an enhancement in activity upon incorporation of small amounts of Rh, despite the fact that Rh₂P prepared similarly is not particularly active. The OER activity was found to increase over time, associated with phase segregation of Rh, suggesting sacrificial depletion of Rh may enhance activity of the Co oxide/hydroxide formed under oxidative conditions. 17-20 As a means to discern how the interplay between the base metal and noble metal governs activity and stability, we seek here to investigate the compositional effects on water splitting catalysis of the nickel analog, Ni_{2-x}Rh_xP. Ni was chosen because it is one of the three base metals (along with Co and Fe) known to form layered double hydroxides that are highly active for alkaline OER catalysis, and because of prior reports of high HER activity in a phosphided RhNi phase under alkaline conditions.²¹

Indeed, the prior study on phosphided RhNi supported on graphene oxide underscores the problems with discerning the innate compositional effects on catalysis in the context of surface area, mediators, and phase/phase purity, while at the same time providing a motivation for evaluating this system for HER.²¹ The phosphided RhNi is not crystalline, nor does it appear compositionally to adhere to the classic 2:1 M:P ratio of the crystalline phases, but it does catalyze HER in alkaline hydrazine more efficiently than the metal alloy.²¹ With that study as inspiration, we report here the first synthesis of discrete Ni_{2-x}Rh_xP nanoparticles and evaluate their composition-dependent electrocatalytic activities towards water oxidation and reduction in alkaline media. A systematic comparison to Co_{2-x}Rh_xP enables us to better define the roles of minority noble metals (Rh) in base-metal phosphides for OER and of minority base metals in noble-metal (Rh) phosphides for HER.

EXPERIMENTAL SECTION

Reagents

Nickel acetylacetonate (Ni(acac)₂, Alfa Aesar, 95%), hydrated rhodium chloride (RhCl₃.nH₂O, Sigma-Aldrich, 38-40% Rh), tri-n-octyl phosphine (TOP, STREM Chemicals, 97%), 1-octadecene

(Sigma-Aldrich, 90%), oleylamine (TCI America, >50%), n-octyl ether (TCI America, 95%), chloroform (Fisher Scientific), hexanes (technical grade, Fisher Scientific), isopropyl alcohol (Sigma-Aldrich, 99.9%), ethanol (200 proof) (Decon Laboratories), Nafion (5%, LQ-1105, Ion Power) and KOH (Sigma-Aldrich, ≥85%, pellets) were used as received.

Synthesis of Ni_{2-x}Rh_xP Nanoparticles

All reactions were carried out under an argon atmosphere using standard Schlenk line techniques. To synthesize Ni_{2-x}Rh_xP (Table S1), the corresponding amount of Ni precursor and Rh precursor in (0.42-x) mmol Ni to x mmol Rh ratio were combined with 15.0 mL of oleylamine (reducing agent and coordinating ligand) and 5.0 mL of 1-octadecene (solvent) in a 200 mL Schlenk flask with an attached condenser. Then the flask was placed on a heating mantle which was connected to a temperature controller. The thermocouple was inserted between the flask and the heating mantle, and the mixture was degassed at 120 °C for 30 min to remove moisture and oxygen. Then argon was purged for 20 min at the same temperature. The temperature was then increased up to 260 °C and maintained for 3 h. After 3 h, 8.0 mL of TOP was quickly injected into the mixture from the top of the condenser using a 12" long needle. Next, the temperature was set to 350 °C and was maintained for another 3 h. After naturally cooling the mixture to room temperature, 20 mL of ethanol was added to the solution and centrifuged to isolate the precipitate. The precipitate was dispersed in 5 mL of chloroform, sonicated for 5 min, and reprecipitated, adding ethanol, followed by centrifugation. This sonication and precipitation process was carried out two times.

Synthesis of Ni₂P Nanoparticles

Ni₂P nanoparticles were synthesized using a method developed by Muthuswami *et al.* with minor variations.²² Ni(acac)₂ (0.59 g), 6.0 mL of oleylamine, 15.0 mL of n-octyl ether and 2.0 mL of TOP was added to a 200 mL Schlenk flask. The mixture was degassed at 120 °C for 30 min, and then argon was purged for 20 min at the same temperature. The temperature was then increased up to 230 °C and maintained for 90 minutes. After 90 minutes, 3.0 mL of TOP was quickly injected into the mixture. Next, the temperature was set to 350 °C and was maintained for another 3 h. After naturally cooling the mixture to room temperature, the sample was purified three times using chloroform and ethanol, as described in the procedure for the synthesis of Ni_{2-x}Rh_xP.

Synthesis of Rh₂P Nanoparticles

Rh₂P nanoparticle synthesis procedure was adopted initially from a method developed by Schaak group, then modified by Mutinda *et al.*^{18,23} RhCl₃.nH₂O precursor (0.1 g), 15.0 mL of oleylamine and 5.0 mL of 1-octadecene was added to a 200 mL Schlenk flask. The mixture was degassed at 120 °C for 30 minutes, and then argon was purged for 20 min at the same temperature. The temperature was then increased up to 230 °C and maintained for 90 minutes. After 90 minutes, 6.0

mL of TOP was quickly injected into the mixture. Next, the temperature was set to 350 $^{\circ}$ C and was maintained for another 3 h. After naturally cooling the mixture to room temperature, the sample was purified three times using chloroform and ethanol, according to the procedure described for the synthesis of $Ni_{2-x}Rh_xP$.

Ink Preparation

50 mg of purified nanoparticles were mixed with 25 mg of Ketjen-300J carbon (C) in hexane and sonicated for 30 min to form C-NPs. The formed C-NPs were then washed with hexane and reprecipitated by centrifugation. The precipitate was then dried under vacuum, followed by annealing in a furnace under 5% H₂/Ar at 400 °C for 1h. An ink was prepared by mixing 15 mg of annealed C-NPs, 2 mL ethanol, 1 mL isopropanol, and 1 mL nano pure water, followed by sonicating for 20 minutes. Then 1 mL of a 5 wt% Nafion solution was added and the mixture was again was sonicated for 20 minutes.

Powder X-ray Diffraction (PXRD)

To collect PXRD patterns, a Bruker D2 Phaser X-ray Powder Diffractometer with Cu Ka radiation (0.154 nm) operated at 30 kV, 10 mA with a step size of 0.02° was used. Nanoparticle samples were placed on a zero-background holder, and data were collected over a 2θ range of 30-60°. PXRD patterns were identified with reference to powder diffraction PDFs from the ICDD database. The Diffraction.Eva v3.1 software was used to calculate the samples' Scherrer crystallite sizes by fitting peak positions and observed maximum angle values given by the software were used to quantify d-spacing changes.

Transmission Electron Microscopy (TEM)

TEM and energy dispersive spectroscopy (EDS) experiments were conducted using a JEOL 2010 electron microscope operating at a voltage of 200 kV and coupled to an EDS detector (EDAX Inc). Bright-field images were collected by Amtv 600 software. EDS elemental mapping data were collected using a JEOL 2100F probe-corrected scanning transmission electron microscope operating at 200 kV and equipped with a high angle annular dark-field (HAADF) and EDAX detectors. For TEM analysis, nanoparticles were dispersed in chloroform, and the solution was sonicated for 20 minutes. A drop of solution was deposited on a formvar carbon-coated 200 mesh Cu grid and allowed to dry completely under air. The particle sizes were calculated using NIS-Elements D3.10 software.

Fourier Transform Infrared Spectroscopy (FT-IR)

To evaluate the efficacy of surfactant removal by annealing during ink processing, we collected IR data before and after the heat treatment using a Bruker Tensor 27 FTIR-spectrometer with OPUS 6.5 software version. The samples were prepared by mixing the composite with dry KBr salt followed by pressing into transparent pellets using a 13 mm die set and a Carver press. IR data were collected and referenced to a blank KBr pellet.

X-ray Photoelectron Spectroscopy (XPS)

A NEXSA, ThermoFisher Scientific instrument was used with a monochromatic Al K α (1486.7 eV) X-ray Source operating at 6 mA and 12 kV. The work function was calibrated to give binding energy of 83.98 eV for Au4f7/2. The spot size is 400 μ m. The surface charges were neutralized using a focused low-energy electron beam. Spectrometer Resolution Details: Ag 3d5/2 core line FWHM at 10 eV pass-energy = 0.5 eV; instrumental resolution = 0.38 eV. XPS was conducted for selected pre-catalyst and post-catalyst samples supported on C cloth. Samples were sputtered at 2 keV with Ar+ for 90 seconds before collecting the spectra. The scan details are shown in Table S2. Thermo Avantage v5.9922 software was used to analyze the collected high-resolution spectra, and binding energies were calibrated against the C 1s peak at 282.8 eV.

Electrochemical Measurements

Cyclic voltammograms were collected using an EC epsilon potentiostat equipped with a rotating disc electrode (RDE) using a standard three-electrode setup. An Ag/AgCl electrode was used as the reference electrode, and the potential was checked against a master Ag/AgCl reference electrode periodically to ensure there is no potential drift from electrode oxidation under strongly alkaline conditions. A carbon electrode was used as the counter electrode for collecting HER polarization curves, while a Pt wire counter electrode was used to collect OER polarization curves. A glassy carbon electrode with a surface area of $0.07~\rm cm^2$ was modified by drop-casting $10~\mu L$ of C-NP ink onto the surface to get a catalytic loading of $0.285~\rm mg/cm^2$. The electrode was then dried under an infrared heat lamp for 2-3 minutes. HER and OER Polarization curves were obtained in $1M~\rm KOH$ electrolyte at a scan rate of $10~\rm mV/s$ with the RDE operating at $1600~\rm rpm$. IR compensation was performed prior to collecting polarization curves by applying IR-COMP using the epsilon software. The potential was measured in reference to the Ag/AgCl electrode and converted to the reversible hydrogen electrode (RHE) scale using the equation $E_{RHE} = E_{Ag/AgCl} + 0.197 + (0.059~x~\rm pH)$.

Double-layer capacitance (C_{dl}) measurements were carried out using the same experimental setup. C_{dl} data were collected pre-catalysis and post-catalysis and the data were used to calculate the corresponding electrochemically active surface area (ECSA) values. Here forward and reverse CV scans were performed at different scan rates (20-100 mV/s) within an energy window of ± 50 mV

of the open circuit potential (OCP). Then the double layer capacitance values for each sample were obtained by plotting the current density difference at the OCP against the scan rates. These data were then used to calculate the ECSA for the different samples as described in the supporting information (S1).

The stability tests were performed in an H-type cell using similar reference electrodes, counter electrodes, and electrolytes in CV measurements. The working electrode was prepared by drop-casting 140 µL of selected catalyst ink on a carbon cloth substrate with a geometric surface area of 1 cm² and dried under an IR lamp (0.280 mg/cm²). Before ink drop-casting, the substrate material was cleaned and preheated at 450 °C for 2 hours under atmospheric air conditions in a furnace to remove any residual organic material. The fabricated carbon cloth electrode with C-NPs was then used to carry out the stability tests by applying a constant potential on the activated working electrode to get a current density ~10 mA/cm²_{geometric} for 10 h. In all cases, a blank experiment was carried out with the working electrode without C-NPs and subtracted to produce the reported data.

Overall water splitting (OWS) activity evaluation was carried out in a two-electrode system, where Ni_{1.75}Rh_{0.25}P and Ni_{0.25}Rh_{1.75}P C-NPs composites were utilized as the anode and cathode electrocatalysts, respectively. The electrodes were prepared as described for the long-term stability tests on carbon cloth. CV data were recorded in a single flask with anode and cathode located approximately 1 cm apart. Subsequently, a long-term stability test was carried out at a constant potential of 1.85 V vs. RHE for 10 hours.

RESULTS AND DISCUSSION

Synthetic Protocol Development

Our approach to the synthesis of Ni_{2-x}Rh_xP, is based on our method established for Co_{2-x}Rh_xP, ¹⁸ where we were able to make a solid-solution over all x. In both cases, we used solution-phase arrested precipitation employing a one-pot two-step process in which the metal precursors, combined in targeted stoichiometric ratios, were allowed to co-reduce in a mixture of oleylamine (which acts as a reducing agent) and the noncoordinating solvent 1-octadecene to form the alloy at an intermediate temperature, followed by injection of the P precursor, trioctylphosphine (TOP), and an increase in temperature to achieve phosphidation. The temperature conditions and concentration of TOP were varied to identify optimal conditions for phase purity (0.2 mmol total metal precursor; 15 mL oleylamine, 5 mL octadecene), although phase purity was not always possible (vide infra). Based on the optimization studies, the targeted metal ratios were obtained with 8 mL of TOP using an alloying temperature of 260 °C and a phosphidation temperature of 350 °C (Table S3). The formation of a Rh-Ni alloy at the intermediate phase, was verified by isolation and characterization (see Figure S1). For comparison of the activity, binary end members Ni₂P and Rh₂P were also synthesized using a modification of standard procedures. ^{18, 22}

Crystal Structure and Morphology

Synthesized Ni_{2-x}Rh_xP nanoparticles with different compositions were characterized for phase purity using PXRD, morphology by TEM, and composition using EDS. Figure 1 shows the PXRD patterns of the targeted phases and Ni₂P and Rh₂P endmembers. Ni₂P and Rh₂P adopt fundamentally different structures: hexagonal (Fe₂P-type) and cubic antifluorite, respectively. Thus, Ni₂P has two metal sites, one with tetrahedral geometry and one with square pyramidal geometry (equally populated) and P occupies the tricapped trigonal prismatic geometry defined by the metal atoms (Figure 1). In contrast, Rh₂P, has only one metal site: tetrahedral holes inside the face-centered-cubic P anionic lattice (Figure 1). Ni_{2-x}Rh_xP nanoparticles are found to adopt the Fe_2P hexagonal structure-type up to x = 1.5, where a mixture of hexagonal and antifluorite form; more Rh-rich phases are exclusively antifluorite. The incorporation of the second metal is manifest in peak shifts associated with expansion of the hexagonal lattice upon Rh incorporation (to lower 2θ), or compression of the antifluorite structure upon Ni incorporation (to higher 2θ), as shown in Figure 2. Intriguingly, while initial incorporation of Rh into Ni₂P results in a quasi linear increase in the d-spacing of the (111) reflection, suggestive of adherance to Vegard's Law, for 0.75 < x < 1.5, the increase in lattice parameters is significantly dampened. At x = 1.5, where two distinct phases are present, the hexagonal (111) lattice parameter decreases to a value intermediate between those recorded for x = 0.25 and x = 0.5. On the other side, as Ni is added to the antifluorite structure type, there is a significant drop in the d-spacing of the (200) reflection upon incorporation of 0.25 Ni (x = 1.75), but hardly any additional compression noted for 0.50 Ni (x = 1.5), where the phase segregation occurs. Clearly, at x = 1.5, the Rh is being partitioned between the two structure types. Nevertheless, the minimal change in lattice parameters between x = 0.75 and x = 1.5suggests the incorporation of Rh into the hexagonal structure is limited. We also noted a subtle enhancement in the intensity of the Ni₂P 110 peak, which is barely discernable in the native structure, upon incorporation of Rh, likely due to the difference in scattering factor between Rh and Ni. An unidentified peak near 37.5° 20 is also noted for these phases and marked with a red asterix. This peak could be attributed to more P-rich phases, as both RhP2 and Rh4P3 have a peak in that area, but in the absence of other peaks, phase identification is speculative.

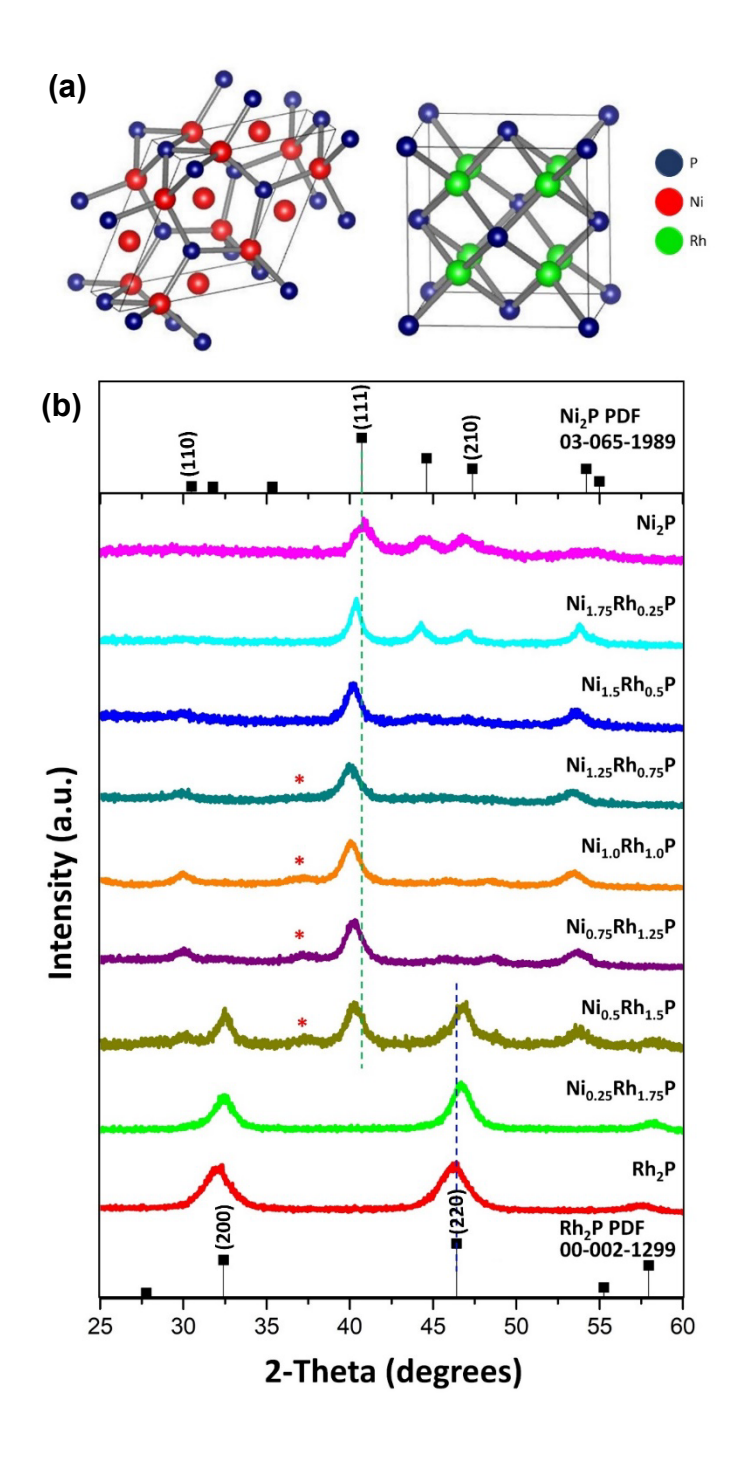


Figure 1. (a) Structure of hexagonal Ni₂P (left) and cubic Rh₂P (right) polymorphs. (b) PXRD patterns for targeted compositions of Ni_{2-x}Rh_xP (x=0-2) nanoparticles. Reference patterns for Ni₂P and Rh₂P are shown with drop lines for major distinguishing peaks. An impurity peak observed for compositions x=0.75-1.5 is indicated with a red asterix.

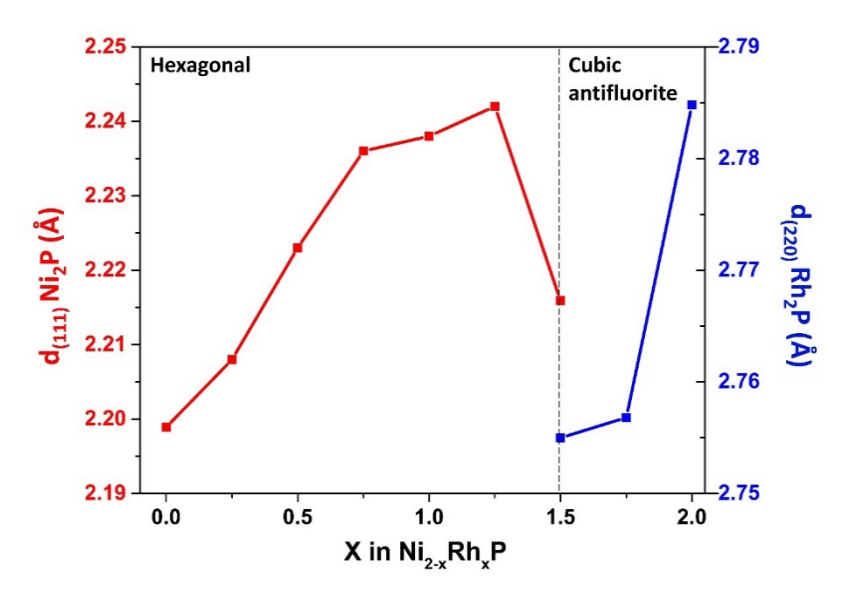


Figure 2. d-spacing change of hexagonal Ni₂P with Rh addition (red) and cubic Rh₂P with Ni addition (blue)

The observation of phase segregation in $Ni_{2-x}Rh_xP$ came as a surprise, as we were able to prepare $Co_{2-x}Rh_xP$ over all x, with the Co_2P -type structure adopted for $x \le 0.75$ and the Rh_2P (antifluorite) type adopted for $x \ge 1$, suggesting a sharp phase transition is occurring for 0.75 > x < 1.0. However, while the structures of Ni_2P and Co_2P are similar in that they have a square pyramidal and tetrahedral site, the arrangement of the polyhedra is not the same, such that Ni_2P is hexagonal (Fe₂P-type) and Co_2P is orthorhombic (Co_2P -type).²⁴ It is possible that these subtle structural differences facilitate miscibility between Co_2P -Rh₂P but inhibit miscibility between Ni_2P -Rh₂P. Alternatively, there may be a competing ternary phase that is more stable, a possibility hinted at by the unidentified peak at near 37.5° 2 Θ (Figure 1). We also considered the possibility that incorporation was limited for intermediate compositions, an effect we have previously observed in MnAs_{1-x}Sb_x nanoparticles.²⁵ In the case of MnAs_{1-x}Sb_x, we noted that As incorporation in MnSb was significantly limited, leading to observed compositions that were considerably As-poor relative to the targeted compositions. This was attributed to differences in relative reactivity. However, EDS data conducted in the TEM for $Ni_{2-x}Rh_xP$ revealed a close agreement between the targeted composition, and the observed composition (see Table 1).

Figure 3 shows the TEM images for Ni_{2-x}Rh_xP, Ni₂P, and Rh₂P nanoparticles. According to the images, Ni₂P nanoparticles have a spherical structure with an average size of 6±1 nm. This value is very close to the crystallite size (6.2 nm) calculated by application of the Scherrer Equation to the (111) reflection, Rh₂P on the other hand has a quasi spherical morphology with an average TEM size of 3±1 and corresponding crystallite size (based on the (220) reflection) of 3.1 nm. As is evident in Figure 3, incorporation of Rh into Ni₂P results in void formation due to the Kirkendall effect, resulting in a larger (more than double) overall particle size (ca 15 nm, Table 1).^{23, 26} This

increase is not wholly attributed to void formation, since the crystallite size computed from the Scherrer equation also increases, albeit by a smaller amount (ca 1.5x). At the other end of the compositional space, incorporation of 12.5% Ni to Rh₂P also results in an increase in particle size of ca 1.5x but without apparent void formation; the crystallite size for the (220) reflection increases proportionally. The phase segregated x=1.5 sample has irregular particles of ca. 14 nm in diameter; some voids are still seen, but otherwise differentiation of particles adopting hexagonal vs. cubic structure is not obvious. Likewise, computed crystallite sizes for hexagonal and cubic are similar (ca 8 nm).

Table 1. Targeted ratios and TEM-EDS ratios (averaged) for Ni_{2-x}Rh_xP nanoparticle compositions. TEM particle size histograms are plotted in Figure S2.

Targeted composition	Average EDS composition	TEM particle size (nm)	Scherrer crystallite size (nm)
Ni ₂ P	$Ni_{2.00(0)}P_{1.07(7)}$	6±1	6.2
Ni _{1.75} Rh _{0.25} P	$Ni_{1.74(2)}Rh_{0.26(2)}P_{0.94(8)}$	15±2	10.7
Ni _{1.50} Rh _{0.50} P	$Ni_{1.51(2)}Rh_{0.49(2)}P_{0.88(9)}$	14±2	9.8
Ni _{1.25} Rh _{0.75} P	$Ni_{1.22(3)}Rh_{0.78(3)}P_{1.21(12)}$	14±2	8.4
Ni _{1.00} Rh _{1.00} P	$Ni_{1.11(7)}Rh_{0.89(7)}P_{1.27(44)}$	15±3	8.3
Ni _{0.75} Rh _{1.25} P	$Ni_{0.75(6)}Rh_{1.25(6)}P_{1.35(45)}$	19±5	8.1
Ni _{0.50} Rh _{1.50} P	$Ni_{0.52(2)}Rh_{1.48(2)}P_{1.33(37)}$	14±5	8.5 and 7.9
Ni _{0.25} Rh _{1.75} P	Ni _{0.26(4)} Rh _{1.74(4)} P _{1.03(15)}	5±1	4.4
Rh ₂ P	Rh _{2.00(1)} P _{0.98(1)}	3±1	3.1

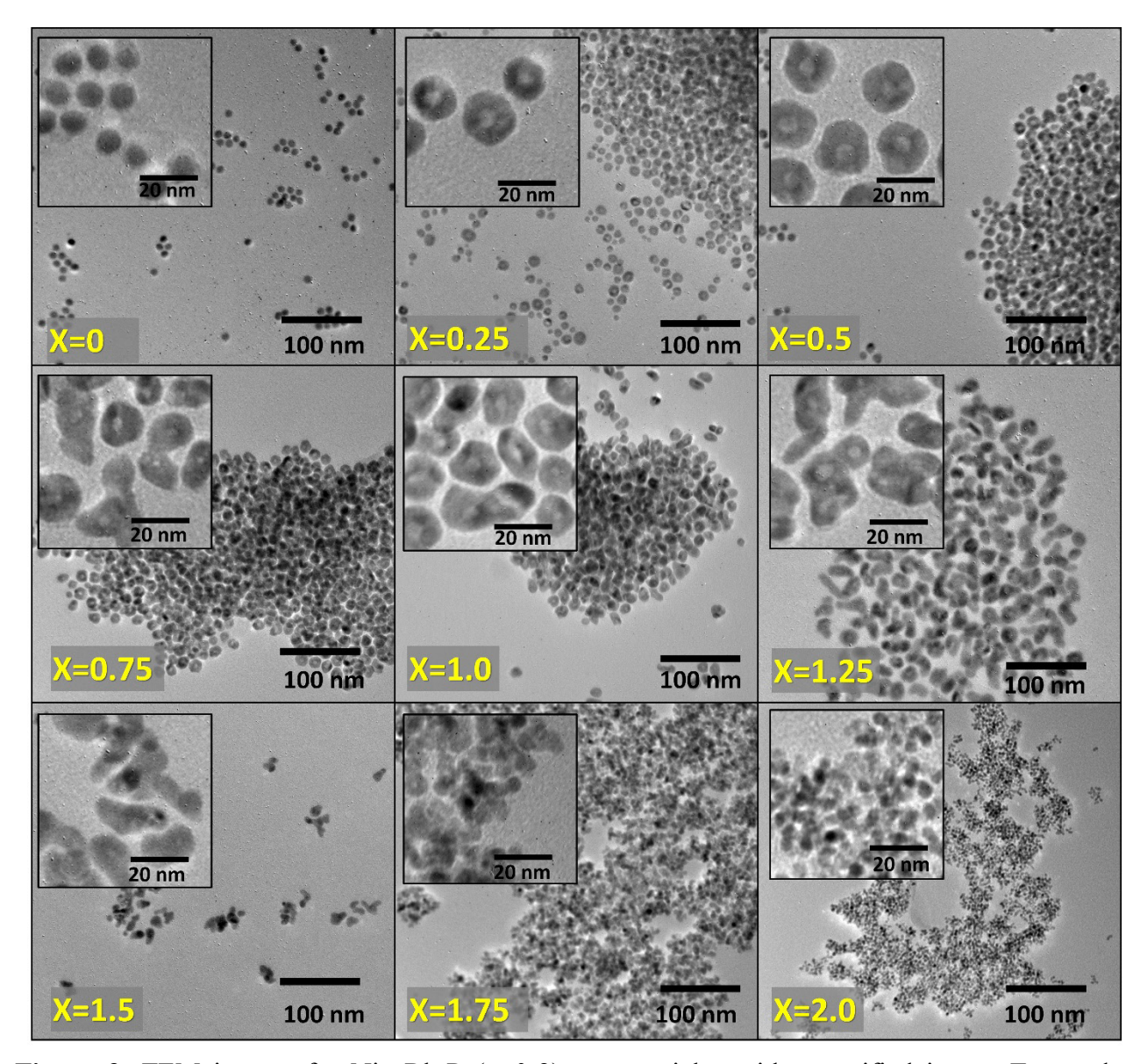


Figure 3. TEM images for $Ni_{2-x}Rh_xP$ (x=0-2) nanoparticles with magnified insets. Targeted compositions are indicated and sizes obtained from the size histograms (depicted in Figure S2) are presented in Table 1

Electrocatalytic Studies

Generally, there is a growing consensus that HER and OER conducted in strongly alkaline media transforms the phosphide precatalysts into oxide/hydroxides. It is an intriguing aspect of these materials that, upon activation, the phosphides outperform deliberately prepared oxide/hydroxide materials.²⁷⁻³¹ It is possible that the differences reflect the reduced "core" of the catalysts produced from phosphides, which may facilitate electron transport to and from the reactive surface.

To evaluate the composition-dependent electrocatalytic activity of Ni_{2-x}Rh_xP, samples deemed to be phase-pure by PXRD (i.e., those on the extreme Ni-rich end and Rh-rich end: x = 0, 0.25, 0.50, 1.75, and 2.0) along with the Ni_{1.0}Rh_{1.0}P composition as a representative of phase segregated and intermediate composition sample, were incorporated into a carbon ink to form Ni_{2-x}Rh_xP C-NPs inks. Before the ink preparation, we annealed the Ni_{2-x}Rh_xP C-NPs composite under reducing conditions. We collected IR data before and after the heat treatment (Figure S3). We observed the disappearance of native peaks at 3300-3500 due to N-H (oleylamine) and C-H (oleylamine, TOP, octylether) stretching. The peak at 1120 due to C-O stretching (octylether) is significantly attenuated after annealing. These data suggest the bulk of the surface ligands have been removed by this process. The prepared Ni_{2-x}Rh_xP C-NPs inks were drop cast onto a glassy carbon rotating disk electrode (mass loading: 0.285 mg/cm², surface area 0.07 cm²). The electrocatalytic OER and HER activity of Ni_{2-x}Rh_xP C-NPs were evaluated in 1M KOH using a three-electrode system.

Figure 4 shows the OER catalytic activity data for Ni_{2-x}Rh_xP C-NPs. A clear oxidation peak that corresponds to NiII to NiIII/IV formation can be observed in our polarization curves at ~1.40 V for Ni-rich phases (Figure 4a), shifted from ~1.44 V in Ni₂P. ^{19, 32, 33} This suggests that Rh incorporation facilitates oxidation of Ni, an unexpected result. From the literature, it is known that *in-situ* formed metal oxides comprise the catalytic surface of phosphide catalysts in alkaline media. ³³ According to our data, when normalized to geometric surface area the Ni_{1.75}Rh_{0.25}P catalyst exhibits the highest OER activity among the investigated electrocatalysts, with an overpotential (η) of 273.1 mV @ 10 mA/cm²_{geo}, (Figure 4b). Unsurprisingly, this composition also exhibits the lowest Tafel slope (30 mV/dec, Figure S4). The slope is consistent with the oxidation of surface metal hydroxide to oxide as the rate-determining step at low surface coverage. ³⁴ All Ni_{2-x}Rh_xP samples outperform a commercial Pt/C catalyst when performed under identical conditions (η = 720 mV @ 10mA/cm²_{geo}, Figure S5).

While the geometry-normalized activity is useful for evaluating device performance, it does not reflect the intrinsic activity because it assumes an equivalent number of available active sites per unit area (or per mg, since we have the same mass loading in each case). Thus, geometric normalized data fails to account for surface roughness associated with sample preparation, composition-dependent variations of particle size (see Figure 3) and sample-to-sample variations in active site density within a specific composition. Accordingly, we measured the electrochemical surface area (ESCA) as a means to assess the average activity per active site. RESA values were calculated from double-layer capacitance measurements (C_{dl})³⁸⁻⁴⁰ conducted at different scan rates in the non-faradaic region (see Figure S6 for C_{dl} plots and SI for detailed ECSA calculation). Because our inks incorporate carbon black, which contributes to the overall conductivity and capacitive behavior, Al, Al, and because side reactions such as corrosion, specific adsorption, intercalation, etc., also can affect these C_{dl} values, Al, we do not purport to report the absolute intrinsic activity and use ECSA only for direct comparison of samples prepared in the same way. We also employ ECSA as a means to probe the stability of the relevant catalysts and understand how they are changed in the catalytic process. We further note that the calculated ECSA values

(Table S4) are much higher than the geometric surface area; hence, we evaluated the overpotential at $2.0 \,\mu\text{A/cm}^2\text{ECSA}$ to compare the catalytic activity.

According to the ECSA normalized data (Figure 4c,d) again, Ni_{1.75}Rh_{0.25}P shows the highest activity, but the activity difference between this phase and the other Ni-rich (hexagonal) phases is enhanced, suggesting a significant intrinsic activity difference not reflected in the geometric surface area normalized data. When we compared the ECSA for the 1st polarization curve vs. the 30th polarization curve, a moderate increment is noted for all of the Ni-rich phases (< 20%). In contrast a significant difference between ECSA (>75% increment after 30 cycles) was observed with Rh-rich cubic Ni_{2-x}Rh_xP compounds (Table S4), reflecting the instability and evident continuous restructuring with oxidation of the Rh rich end.

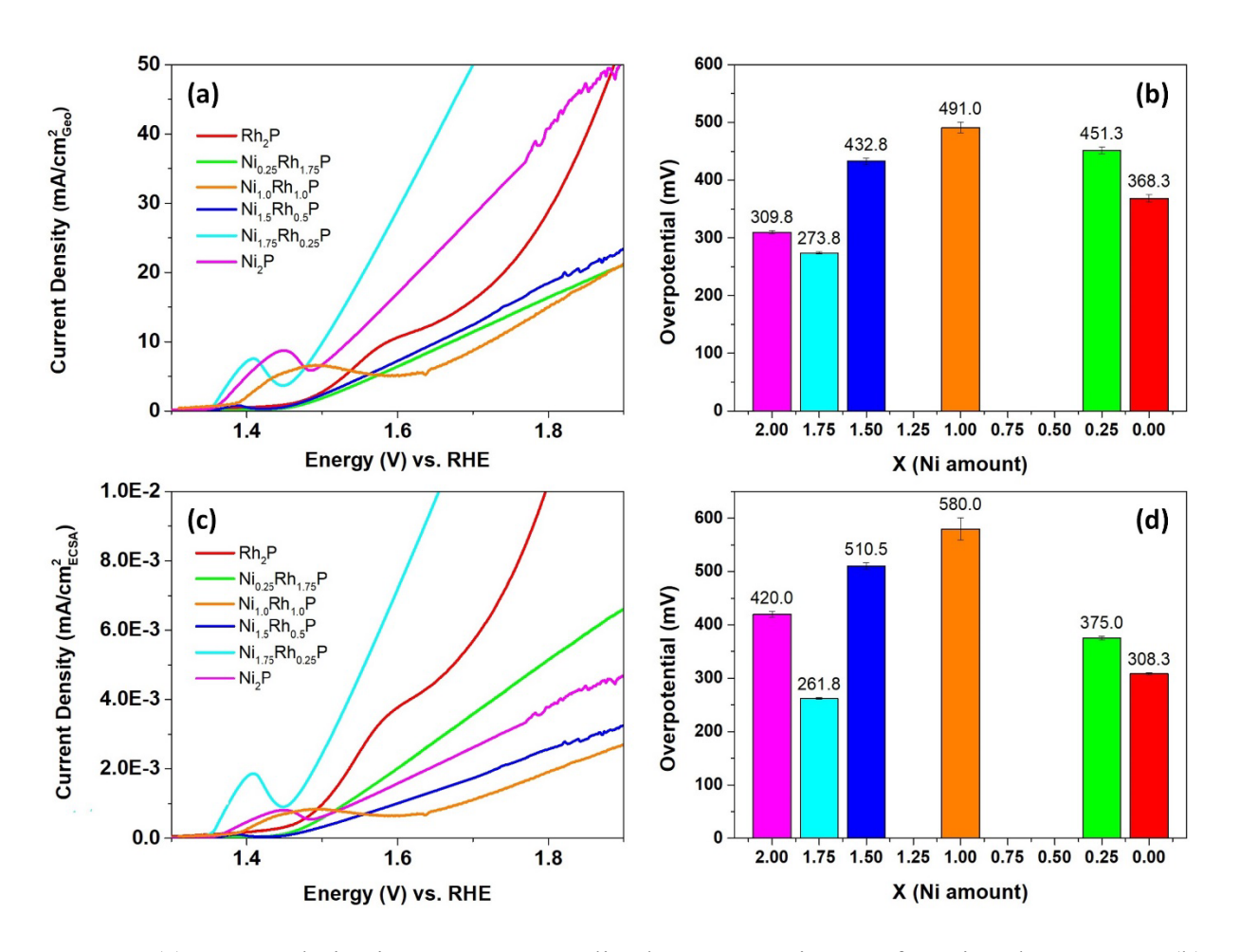


Figure 4. (a) OER polarization curves normalized to geometric area for Ni_{2-x}Rh_xP C-NPs. (b) Overpotentials at 10 mA/cm²_{geo}. (c) OER polarization curves normalized to ECSA for Ni_{2-x}Rh_xP C-NPs. (d) Overpotentials at 2.0 μA/ cm²_{ECSA}.

HER catalytic activity data are presented in Figure 5. As expected, the Rh-rich phases are more active, with Rh₂P ($\eta = 66.2 \text{ mV}$ @ 10mA/cm^2_{geo}) outperforming the modestly doped ternary phase

 $Ni_{0.25}Rh_{1.75}P$ (η = 82.1 mV @ 10mA/cm²_{geo}). With the exception of Ni_2P and $Ni_{1.75}Rh_{0.25}P$, all compositions outperform the commercial Pt/C standard (n= 135 mA @ 10mA/cm²geo, Figure S5). The Tafel slopes of Rh₂P (56 mV/dec) and Ni_{0.25}Rh_{1.75}P (63 mV/dec) are close to the expected value for a rate-limiting chemical step preceded by electron transfer (59 mV/dec),⁴⁴ whereas the slopes of the more Ni-rich phases are considerably higher, ranging from 84-112 mV/dec. Intriguingly, when normalized to ECSA, the overpotential of the Ni_{0.25}Rh_{1.75}P phase is half that of Rh₂P (44.5 vs. 88.0 mV @ 2 μA/cm²_{ECSA}). According to the literature, the water dissociation step associated with HER in alkaline media can occur on Ni(OH)2 and then facilitate the production of hydrogen intermediates adsorbed to the surface of neighboring noble metal active sites to yield molecular hydrogen.⁴⁵ A similar phenomenon might be happening on the Ni_{0.25}Rh_{1.75}P surface. Thus, even though the ternary phase necessarily has a lower number of Rh sites than Rh₂P, the overall higher site activity suggested by the ECSA might be a consequence of a lowering of the energy barrier in the water dissociation step. We also noted an increment in ECSA after 30 cycles of HER, but the changes are moderate for the most active Rh-rich phases (<20%, Table S4). Alternatively, it is possible that the large ECSA obtained upon Ni incorporation reflects sites that are electrochemically active, but not catalytically active.

The targeted 1:1 metal composition phase was also evaluated for both OER and HER activity (Figure 5 and 6) to establish whether phase-segragation positively effects the activity, which would motivate a more detailed evaluation of the fellow intermediate composition phase-segregated samples. We did note in OER studies that the Ni_{1.0}Rh_{1.0}P sample has an excessively broad (>200 mV) peak associated with the NiII to NiIII/IV couple that is shifted to higher potential, ~1.48 V, relative to other phases (Figure 4) demonstrating unique behavior that may be associated with the impurity phase observed by PXRD (Figure 1). However, for both geometric activity and the ECSA normalized activity, the observed overpotential values for OER and HER were not competitive with the more active phases. Therefore, further evaluation of phase-segregated samples was not carried out.

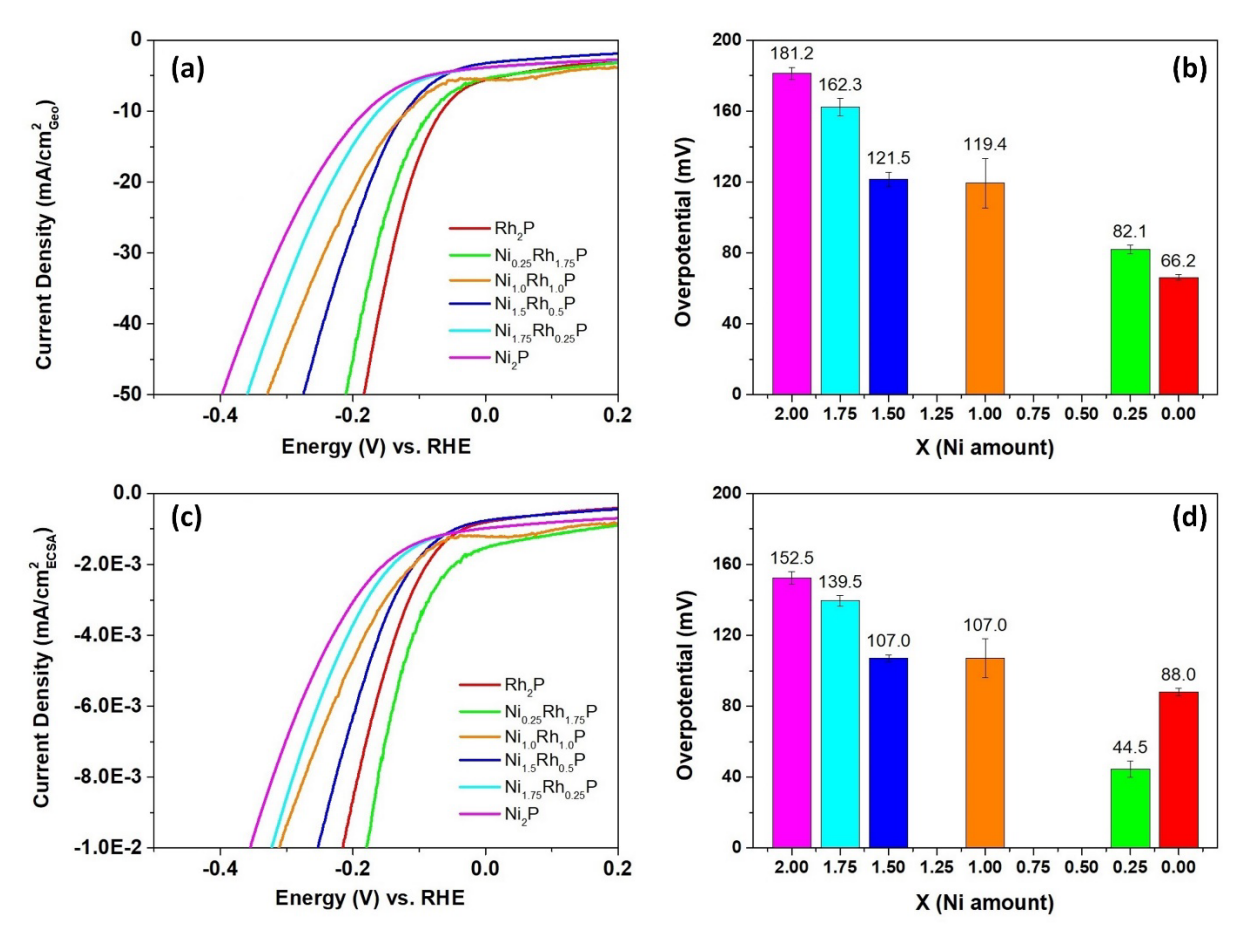


Figure 5. (a) HER polarization curves normalized to geometric area, for Ni_{2-x}Rh_xP C-NPs. (b) Overpotentials at -10 mA/cm²_{geo}. (c) HER polarization curves normalized to ECSA for Ni_{2-x}Rh_xP C-NPs. (d) Overpotentials at -2.0 μA/cm²_{ECSA}.

To evaluate the stability of the catalysts, long-term stability measurements were collected on the composition with the highest intrinsic activity for OER and HER. As shown in Figure 6, the geometric activity of Ni_{1.75}Rh_{0.25}P shows a 6% increase after 10 h in the basic medium for OER while Ni_{0.25}Rh_{1.75}P shows a 22% activity decrease after 10h for HER. To better understand how restructuring might be affecting the intrinsic properties, we also compared the ECSA values (Figure S7, Table S5) and ECSA normalized current density data (Figure 6) before and after the 10 h runs. We observed that the changes in device performance (geometrical) are reflecting intrinsic changes in the catalyst; i.e., a decrease (OER, 0.7x) or increase (HER, 1.5x) in ESCA over the course of the 10 h catalytic study. To discern the nature of these changes, we probed localized and surface compositional/speciation changes using STEM-EDS mapping and XPS before and after the 10 h stability cycles.

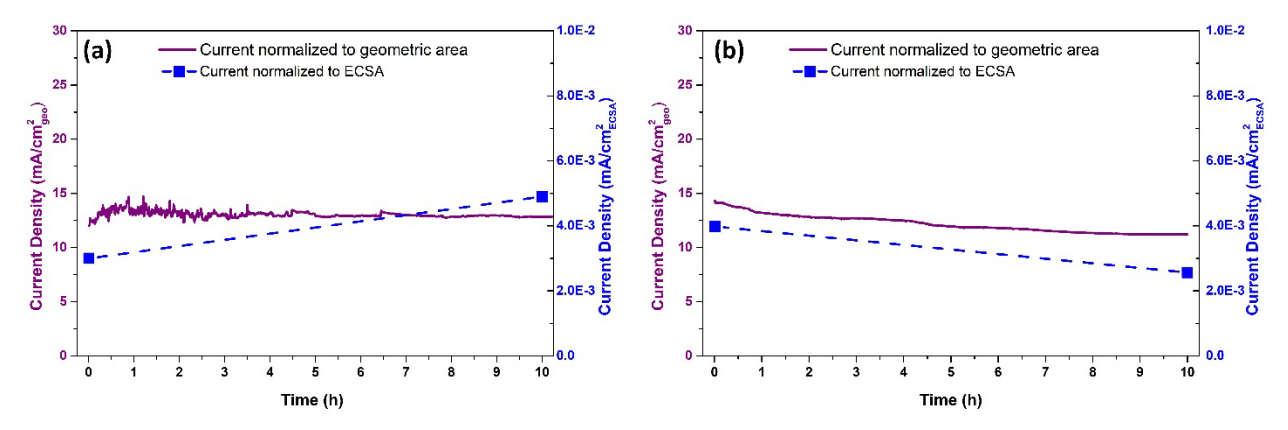


Figure 6. Long-term stability test for (a) Ni_{1.75}Rh_{0.25}P for OER at 1.5 V (b) Ni_{0.25}Rh_{1.75}P for HER at 0.085 V. The blue squares represent the current normalized to ECSA before and after the stability test. The blue dotted lines are a guide for the eye.

We also tested the electrolytic performance of Ni_{2-x}Rh_xP C-NPs composite towards overall water splitting, an overall water electrolyzer was prepared in a two-electrode configuration. Ni_{1.75}Rh_{0.25}P and Ni_{0.25}Rh_{1.75}P C-NPs ink were used to prepare the anode and cathode, respectively. In order to lower the overall cell resistance, the anode and cathode electrodes were kept close to each other with no membrane separator (Figure S8). The electrolytic activity of the overall cell was evaluated by collecting a cyclic voltammogram to determine the potential required to achieve a current density of 20 mA/cm²geometric (Figure 7a). The overall cell potential to deliver 20 mA/cm²geometric was 1.78 V (without IR correction). This value was slightly higher than the sum of the HER and OER half-cell reactions values to achieve 20 mA/cm²geometric (1.69 V, with IR correction). This difference might be due to the cell resistance.

As shown in Figure 7b), the electrochemical stability of the overall cell was also evaluated at a constant potential of 1.85 V for 10 hours. The current density was found to decrease by 19.6% over time, which we attribute to deactivation of the cathode as observed in the HER stability test (Figure 6b).

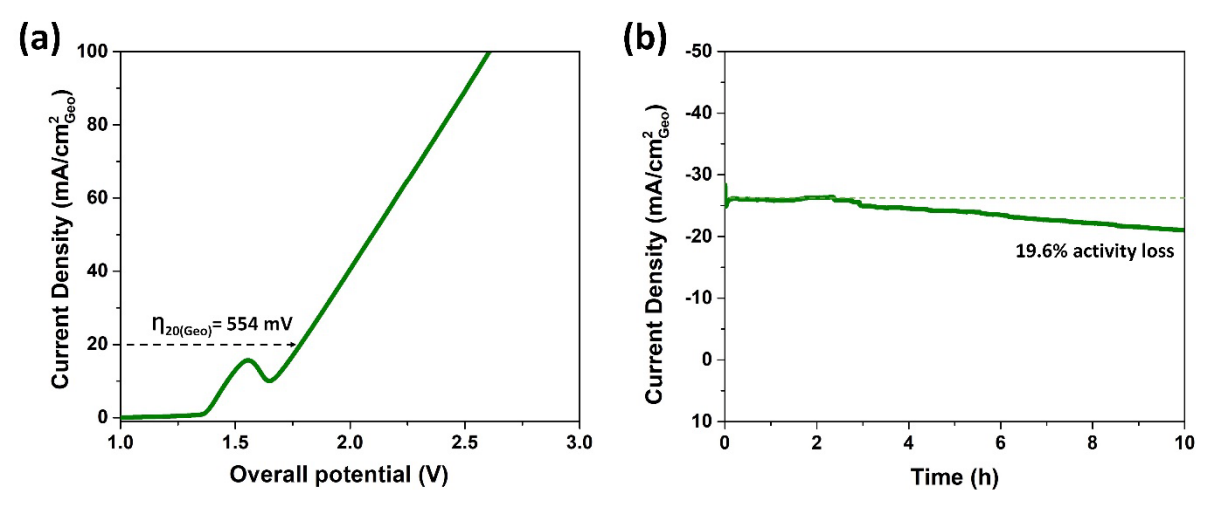


Figure 7. Overall water splitting of the cell Ni_{1.75}Rh_{0.25}P/C \parallel Ni_{0.25}Rh_{1.75}P/C (a) activity and (b) stability data at 1.85 V.

Structural elucidation: STEM-EDS mapping and XPS

According to STEM-EDS mapping images in both compositions, Ni, Rh, and P were uniformly distributed in the structure of the nanoparticles before catalysis (Figure 8a, 8c). After 10 h of catalytic activity, the channel for oxygen, which displayed uniform intensity before catalysis (See Figure 8a, 8c) now shows O to be co-localized on the nanoparticles (Figure 8b, 8d). Intriguingly, the Ni_{1.75}Rh_{0.25}P sample showed evidence of Rh segregation in high resolution images conducted after OER (Figure S9), whereas the elemental components in the Ni_{0.25}Rh_{1.75}P sample were still uniformly distributed after HER (Figure 8d).

To better understand how the active surfaces are changing upon OER and HER catalysis, and aid in contextualizing the STEM-EDS data, XPS analyses were also carried out before and after the 10 h stability test using Ni_{1.75}Rh_{0.25}P and Ni_{0.25}Rh_{1.75}P containing inks, respectively.

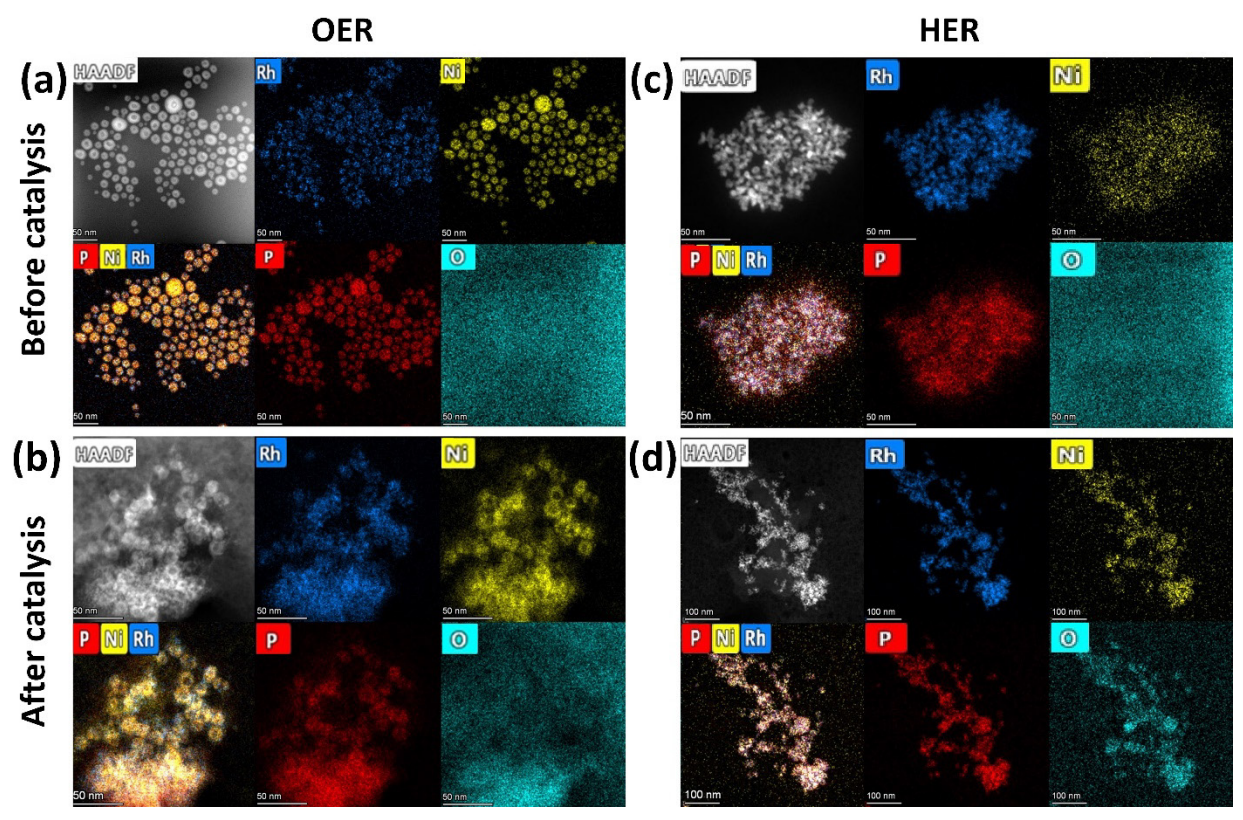


Figure 8. EDS mapping analysis of Ni_{1.75}Rh_{0.25}P C-NPs (a) before and (b) after OER activity and Ni_{0.25}Rh_{1.75}P C-NPs (c) before and (d) after HER activity.(Scale bar is 50 nm in a-c and 100 nm in d)

Figure 9a summarizes the XPS spectra of Ni 2p, Rh 3d, P 2p, and O 1s, before and after the 10 h OER stability test for Ni_{1.75}Rh_{0.25}P. According to the EDS elemental analysis (in TEM) of the fresh ink, the nanoparticles have a bulk composition of Ni_{1.74}Rh_{0.26}P_{0.94} (Table 2). However, the surface composition elicited from XPS is quite different, with M/P = 5.3 vs. 2.0 ideal, and only a trace of Rh (not quantified). The pre-catalyst has Ni 2p_{3/2} peaks at 853.5 eV and 856.3 eV, attributed to metallic nickel bound to phosphorous and Ni²⁺ from oxides/hydroxides, respectively. 46 Satellite peaks of the Ni spectrum can be seen at 860.4 eV and 863.5 eV.⁴⁷ The surface signals for Rh 3d were very weak as there is a low amount of Rh in the composition and, possibly, Rh is underrepresented on the surface. The Ni₂P surface is known to be readily oxidized and moisture adsorbing, forming NiO and Ni(OH)₂ when exposed to the atmosphere. ⁴⁸⁻⁵⁰ Our data also suggest that the surface of Ni_{2-x}Rh_xP is susceptible to air oxidation and atmospheric moisture adsorption resulting in an Ni⁰/Ni²⁺ ratio of 0.79 (Table 3). Likewise, the P spectrum shows two doublet peaks at 129.9 eV and 133.6 eV for reduced phosphorus (in the metal phosphide) and phosphate, 47,51 respectively, and the O1s spectrum confirms metal oxides at 531.8 eV. An additional peak at 533.8 eV in the O1s spectrum is attributed to C-O due to Nafion in the ink and/or surface hydroxide groups. 47, 52, 53

After catalysis, the overall bulk composition by EDS (TEM) reveals minimal changes in the Ni:Rh ratio, but a significant depletion (~48%) in P (Ni_{1.73}Rh_{0.27}P_{0.45}). However, the surface XPS data shows the presence of 2% Rh, and 98% Ni, with no detectable P. Leaching of phosphorus as phosphate is expected as the surface becomes oxidized. Likewise, the presence of metallic Ni on the surface is significantly depleted due to oxidation (Ni⁰/ Ni²⁺ = 0.05, Table 3). Another new peak at 858.4 eV is visible in the spectrum, which we attribute to Ni³⁺ resulting from electrochemical oxidation of Ni²⁺.^{54, 55} Interestingly, after catalysis the Rh spectrum is better resolved, enabling clear fitting. This may be a consequence of the segregation noted in the STEM-EDS (see Figure S9). In contrast to Ni, the Rh appears unoxidized post OER.

Table 2. EDS and XPS elemental ratios before and after the 10 h catalytic stability test (see Table S6 for quantified values).

Composition	Status	EDS (bulk)		XPS (surface)	
		Ni:Rh	M:P	Ni:Rh	M:P
Ni Dh D	Before OER	87:13	68:32	100:0	84:16
Ni _{1.75} Rh _{0.25} P	After OER	87:13	82:18	98:2	100:0
Ni _{0.25} Rh _{1.75} P	Before HER	13:87	66:34	66:34	88:12
1N10.25K111.75F	After HER	15:85	70:30	81:19	100:0

Table 3. XPS ratios of oxidation states of each element before and after the 10 h catalytic stability test (see Table S7 for quantified values).

Composition	Status	Ni: Ni ^{2+/3+}	Rh:Rh ³⁺	P:PO4 ³⁻
Ni _{1.75} Rh _{0.25} P	Before OER	44:56	ND	25:75
1N11.751X110.25F	After OER	5:95	100:0	ND
Ni _{0.25} Rh _{1.75} P	Before HER	12:88	39:61	15:85
	After HER	6:94	14:86	ND

Figure 9b summarizes the XPS data before and after the 10 h stability test for HER activity. XPS analysis of the fresh catalyst reveals Ni 2p_{3/2} peaks at 853.8 eV and 856.5 eV for Ni-P and Ni²⁺ respectively.⁴⁷ There is also an intense peak at 858.7 eV for Ni³⁺, distinctly different from the Ni-rich phase studied for OER where Ni³⁺ is only observed post-catalysis (see Table S7). This Ni³⁺ peak is reminiscent of those reported for Pd bonded Ni surfaces (862.0 eV) and Fe-Ni-S (858.5 eV) surfaces, wherein the Ni electron density is appropriated in bonding to Pd or Fe-S.^{54, 56} In our case, we attribute it to Ni bonded to both Rh and P as the sample is Rh rich. The Rh 3d_{5/2} spectrum has peaks at 307.6 eV and 308.8 eV attributed to Rh⁰ (in the phosphide) and Rh³⁺(Rh₂O₃),

respectively, as well as an additional peak at 310.7 eV that cannot be definitively interpreted, but may by a satellite peak associated with Rh₂O₃.^{47, 57} The P spectrum peaks at 129.6 eV and 133.9 eV indicate reduced phosphorus (in the metal phosphide) and phosphate, respectively. The O1s spectrum confirms the presence of metal oxides (531.6 eV).

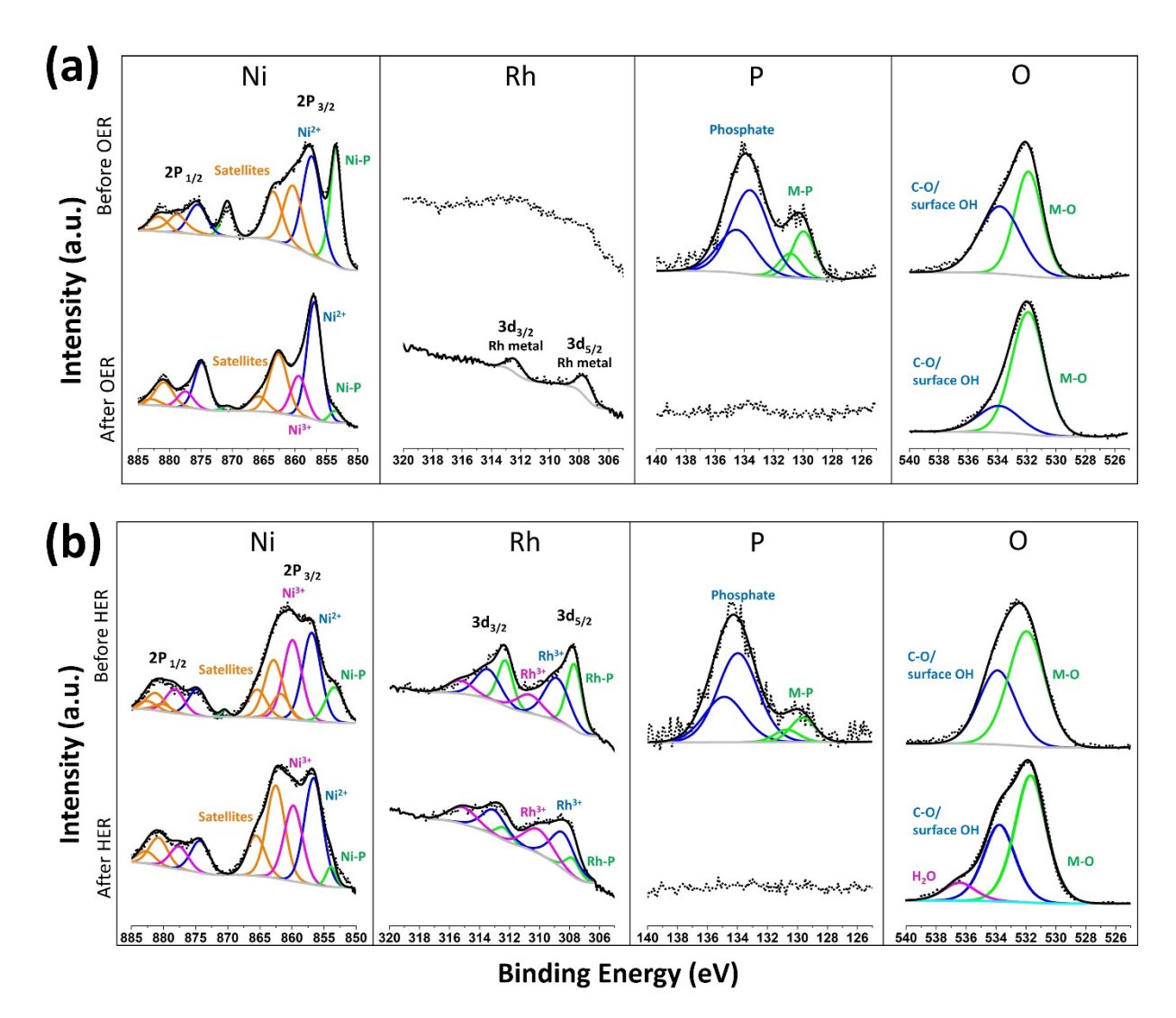


Figure 9. (a) XPS spectra of Ni_{1.75}Rh_{0.25}P C-NPs before and after 10 h OER activity testing (b) XPS spectra of Ni_{0.25}Rh_{1.75}P C-NPs before and after 10 h HER activity testing.

Even though the bulk composition of the catalyst according to TEM/EDS elemental analysis is $Ni_{0.26}Rh_{1.74}P_{1.03}$, the XPS analysis shows the surface is surprisingly Ni-rich (Ni/Rh = 1.9 vs. 0.15 ideal), and, as with the $Ni_{1.75}Rh_{0.25}P$ sample, phosphorus deficient (M/P = 7.3). The origin of the Ni-enhancement at the surface noted for both phases may be a function of differing diffusion energies, surface energies (due to preferred faceting and/or dictated by surface ligands used in the synthesis), and/or defects, etc.⁵⁸ We note that a similar trend was observed for $Co_{0.75}Rh_{1.25}P$: Rh

and P are deficient at the surface relative to the base metal, Co, although the differences are less pronounced than for Ni (Co/Rh = 1.3 vs. 0.6 ideal; M/P = 3.6 vs. 2.0 ideal).¹⁷

After HER catalysis, the only significant change in bulk composition is a decrease of P by 15%, $(Ni_{0.29}Rh_{1.71}P_{0.88})$, suggesting overall P losses are not as great for HER relative to OER. However, according to the XPS data, the surface P is completely depleted, as it was for $Ni_{1.75}Rh_{0.25}P$ post OER, consistent with phosphate displacement by hydroxide species during electrochemical cycling in alkaline media.⁵⁹ Intriguingly, the surface has become even more Ni-rich (Ni/Rh = 4.3), and both Ni and Rh are present mostly in oxidized form $(Ni^0/Ni^{2+/3+} = 0.06; Rh^0/Rh^{3+} = 0.16, Table 3)$.

Assessing the Role of Noble and Base Metal Components in Water-splitting Catalysis over Bimetallic Phosphides

The combined STEM/EDS and XPS data suggest that (1) the surface composition of Ni_{2-x}Rh_xP is quite different from the bulk (targeted) composition with Ni exhibiting a superabundance relative to Rh and P; and (2) Ni_{2-x}Rh_xP undergoes dramatic *in-situ* chemical modifications during both HER and OER processes. In both cases, the initial phosphide/phosphate on the pre-catalytic surface readily oxidizes and then dissolves in the basic electrolyte solution as metal oxides/hydroxide species are formed, as evidenced by the complete disappearance of a P signal in the XPS combined with losses of 15% (HER) to 48% (OER) of P relative to Rh+Ni in STEM/EDS bulk analysis. This loss of phosphide (as phosphate) is by now a generally recognized characteristic of phosphide catalysts for water-splitting reactions in alkaline media. ⁵⁹⁻⁶² However, the nature of the *in situ* changes depends significantly on the native metal composition, surface characteristics, and electrocatalytic treatment (OER vs. HER), which dictates the overall performance and stability.

For the case of Ni_{1.75}Rh_{0.25}P employed for OER at pH = 14, the enhancement in activity upon incorporation of 12.5 % Rh in Ni₂P relative to Ni₂P may be attributed to electronic effects and/or restructuring of the catalyst due to phase-segregation of Rh (Figure S9). The polarization curve provides strong evidence that the presence of Rh shifts the oxidation potential of Ni to lower values, facilitating its oxidation. At the same time, the fact that the Rh, barely detectible and not quantifiable pre-catalysis, is in its reduced state after catalytic testing (Figure 9a) and also physically separated from Co in the STEM/EDS mapping post-catalysis (Figure S9), is a strong indicator that the role of the Rh in promoting catalysis may be changing over time. The consequence of the Rh segregation is a decrease in the ECSA (0.7x vs. pre-catalysis), but at the same time, the ECSA normalized current density is increasing (1.5x vs. pre-catalysis, Figure 6, Table S5). The correlation of Rh phase segregation to decreased electrochemically active surface area, but enhanced catalytic activity, suggests the catalytic sites have become intrinsically more active over the course of catalytic testing. The activity trend dominates the surface area trend, such

that a modest increase in geometric activity (ca 6%) is noted over the course of the 10 h study. We noted a similar trend in OER studies of Co_{1.75}Rh_{0.25}P—the geometric activity is augmented over time and phase-segregation of Rh is evident. This may be due to reconstruction of the base metal catalyst. Alternatively (or, in addition), the segregation of Rh might be a consequence of low—but not zero—solubility of Rh in the reconstructed oxide/hydroxide; i.e., some Rh may remain dispersed and may continue to moderate the activity of the base metal.

For $Ni_{0.25}Rh_{1.75}P$ employed for HER at pH = 14, the case is quite different. Notably, the ECSA increases over time, both at short times (30 cycles, 1.1x, Table S4) and long times (10 h, 1.4x, Table S5). These data correlate to oxidation of Ni to Ni^{2+/3+} and Rh to Rh³⁺, according to XPS data. At the same time, the ECSA normalized current density at 0.85 V is decreasing (Figure 6), suggesting that the overall enhancement in number of electroactive sites actually results in an overall decrease in the per site activity, or that new sites that form in situ are not contributing to the overall catalysis. However, when combined with the fact that the geometrically normalized activity also decreases (Figure 6), it is clear that the catalyst is deactivating, i.e., either the number of active sites—or their potency, is diminished This may be a consequence of Ni replacing Rh (so that Ni is 81% by XPS) on a surface that started out already Ni-rich relative to the bulk composition (66% Ni by XPS vs. 12.5% Ni by TEM/EDS). Given that Rh₂P is reported to be more active than Ni₂P for HER, a decrease in the Rh content would be consistent with a decrease in the number of active catalytic sites. What is not clear is why the addition of Ni leads to enhancement in activity relative to Rh₂P itself, especially given the disproportionately large amount of Ni on the surface relative to the bulk composition. On the other hand, as previously mentioned, the "enhanced" activity is not seen in the geometrically normalized data, only in the ECSA-normalized data. Thus, the Ni may enhance the number of electrochemically active surface sites without playing a proportionate role in the catalytic reaction—or possibly any role. It is also possible that Ni may aid in initial restructuring, which leads to a higher ECSA-normalized current density than for Rh₂P itself (at least initially) or that Rh and Ni work synergistically, with activity loss over time a consequence of the changing surface ratio. However, it is clear that while addition of Ni seems to "goose" the initial activity of Rh₂P, this is achieved by sacrificing long-term stability.

Whereas the behavior of Rh-incorporation on base metal phosphides seems to be similar under alkaline OER conditions for Ni₂P vs. Co₂P, this is not the case for HER catalysis involving incorporation of base metals into Rh₂P; the behavior of Ni_{0.25}Rh_{1.75}P is distinct from that of the Co analog (Co_{0.25}Rh_{1.75}P). When normalized to geometric surface area, Ni_{0.25}Rh_{1.75}P demonstrates a larger overpotential—by 20 mV—relative to Rh₂P or Co_{0.25}Rh_{1.75}P. This may be due to differences in the electronic structure of the bulk; however, XPS data suggest that surface effects may be responsible. Notably, the surface of Ni_{0.25}Rh_{1.75}P has twice as much Ni as Rh, whereas for Co_{0.25}Rh_{1.75}P, the Co is barely evident in the XPS—indeed it is of too low a concentration to obtain a reliable fit.²⁰ The excess Ni at the surface may reflect solubility challenges of Ni incorporation into Rh₂P, as reflected in the lack of solid solution formation across intermediate values of x. Thus,

the surfaces of Ni_{0.25}Rh_{1.75}P and Co_{0.25}Rh_{1.75}P differ considerably in their base metal-to-Rh composition, making an apples-to-apples comparison of the two phases questionable. Additionally, in Co_{0.25}Rh_{1.75}P the Rh remains metallic,²⁰ even as surface phosphide is oxidized and dissolved as phosphate, whereas in Ni_{0.25}Rh_{1.75}P the Rh is largely oxidized, despite the fact that HER is conducted at a more negative potential (by 25mV) for the Ni analog relative to the Co analog. The differences in the behavior of Ni and Co analogs are much greater than would be anticipated based on their atomic properties, underscoring the importance of experimental validation.

CONCLUSIONS

Phase pure $Ni_{2-x}Rh_xP$ colloidal nanoparticles (x=0.25, 0.5, and 1.75) can be prepared with low polydispersity by solution-phase arrested precipitation reactions. Although the synthetic method incorporates an early Ni-Rh alloying step, and the bulk compositions mirror the targeted compositions, the surface compositions of the prepared nanocrystals have a superabundance of Ni relative to Rh and P. When employed as pre-catalysts in alkaline media for water oxidation and reduction, the most active phases (current density normalized to ECSA) are x = 0.25 and x = 1.75, respectively. However, the origin of the activity and the effect of restructuring on the stability is different. OER reactions (x = 0.25) demonstrate an augmented activity over time at 1.505 V, whether normalized to geometric surface area or ECSA, and this correlates to phase segregation of metallic Rh. In contrast, HER reactions (x = 1.75) undergo a decrease in ECSA-normalized and geometrically normalized current densities at 0.85 V over time. In comparing to prior work from our lab on the related Co_{2-x}Rh_xP nanoparticles, we find that the role of Rh as an "activator" for the base metal oxide is the same in both cases (likely driven by phase-segregation), whereas Co is distinct from Ni when incorporated into Rh₂P at similar bulk concentrations, in that the Co does not preferentially segregate to the surface (or does so on a much smaller scale), leaving the more active (and stable) Rh component to dominate despite being diluted by a base metal. Current studies are focused on understanding the role of Rh phase-segregation in OER activation, specifically with an eye towards discovery of alternative "activating" elements (ideally non-noble), and assessing how synthetic factors affect the surface composition of bimetallic phosphides to enable "selective surfaces".

ASSOCIATED CONTENT

Supporting Information

Experimental details on electrochemically active surface area (ECSA) calculations. Figures comprising the PXRD pattern for isolated Ni-Rh alloy; particle size histograms for Ni_{2-x}Rh_xP nanoparticles; IR spectra before and after annealing of the C-NPs composite; Tafel plots; 20%Pt/C electrocatalytic activity data; Double-layer capacitance plots; Overall water splitting setup; EDS

mapping analysis of Ni_{1.75}Rh_{0.25}P C-NPs before and after OER activity. Tables of quantities of metal precursors employed in the synthesis of Ni_{2-x}Rh_xP nanoparticles; Scan details for XPS; EDS, ECSA, and XPS data. The Supporting Information is available free of charge at https://pubs.acs.org

AUTHOR INFORMATION

Corresponding Author

Stephanie L. Brock—Department of Chemistry, Wayne State University, Detroit, MI 48202, USA; orchid.org/0000-0002-0439-302X; Email: sbrock@chem.wayne.edu

Authors

Tharanga N. Batugedara—Department of Chemistry, Wayne State University, Detroit, MI 48202, USA

Funding

This work has been supported by the National Science Foundation under grant numbers 1904775, 1361741, 1849578, 0216084, and 1427926.

Notes

The authors declare no competing financial interest.

ACKNOWLEDGMENT

We thank Dr. S. I. Mutinda for conducting preliminary experiments and fruitful discussions and the National Science Foundation (NSF) for support (DMR-1904775 and CHE-1361741). This work employed UPS/XPS, TEM, and PXRD, housed in the Lumigen Instrument Center, Department of Chemistry, Wayne State University, and the Michigan Center for Materials Characterization at the University of Michigan. The UPS/XPS, JEOL-2010 TEM, and PXRD facilities at Wayne State are partially supported by NSF (grant numbers: 1849578, 0216084, and 1427926, respectively).

REFERENCES

- 1. Suen, N.-T.; Hung, S.-F.; Quan, Q.; Zhang, N.; Xu, Y.-J.; Chen, H. M., Electrocatalysis for the oxygen evolution reaction: recent development and future perspectives. *Chem. Soc. Rev.* **2017**, *46*, 337-365.
- 2. Wei, J.; Zhou, M.; Long, A.; Xue, Y.; Liao, H.; Wei, C.; Xu, Z. J., Heterostructured Electrocatalysts for Hydrogen Evolution Reaction Under Alkaline Conditions. *Nanomicro Lett* **2018**, *10*, 75.

- 3. Liu, P.; Rodriguez, J. A., Catalysts for Hydrogen Evolution from the [NiFe] Hydrogenase to the Ni₂P(001) Surface: The Importance of Ensemble Effect. *J. Am. Chem. Soc.* **2005**, *127*, 14871-14878.
- 4. Popczun, E. J.; McKone, J. R.; Read, C. G.; Biacchi, A. J.; Wiltrout, A. M.; Lewis, N. S.; Schaak, R. E., Nanostructured Nickel Phosphide as an Electrocatalyst for the Hydrogen Evolution Reaction. *J. Am. Chem. Soc.* **2013**, *135*, 9267-9270.
- 5. Shi, Y.; Zhang, B., Recent advances in transition metal phosphide nanomaterials: synthesis and applications in hydrogen evolution reaction. *Chem. Soc. Rev.* **2016**, *45*, 1529-1541.
- 6. Pu, Z.; Liu, T.; Amiinu, I. S.; Cheng, R.; Wang, P.; Zhang, C.; Ji, P.; Hu, W.; Liu, J.; Mu, S., Transition-Metal Phosphides: Activity Origin, Energy-Related Electrocatalysis Applications, and Synthetic Strategies. *Adv. Functional Mater.* **2020**, *30*, 2004009.
- 7. Ying, J.; Wang, H., Strategies for Developing Transition Metal Phosphides in Electrochemical Water Splitting. *Front. Chem.* **2021**, *9*, 700020-700020.
- 8. Habas, S. E.; Baddour, F. G.; Ruddy, D. A.; Nash, C. P.; Wang, J.; Pan, M.; Hensley, J. E.; Schaidle, J. A., A Facile Molecular Precursor Route to Metal Phosphide Nanoparticles and Their Evaluation as Hydrodeoxygenation Catalysts. *Chem. Mater.* **2015**, *27*, 7580-7592.
- 9. Mendoza-Garcia, A.; Su, D.; Sun, S., Sea urchin-like cobalt–iron phosphide as an active catalyst for oxygen evolution reaction. *Nanoscale* **2016**, *8*, 3244-3247.
- 10. Zhang, Y.; Li, N.; Zhang, Z.; Li, S.; Cui, M.; Ma, L.; Zhou, H.; Su, D.; Zhang, S., Programmable Synthesis of Multimetallic Phosphide Nanorods Mediated by Core/Shell Structure Formation and Conversion. *J. Am. Chem. Soc.* **2020**, *142*, 8490-8497.
- 11. El-Refaei, S. M.; Russo, P. A.; Pinna, N., Recent Advances in Multimetal and Doped Transition-Metal Phosphides for the Hydrogen Evolution Reaction at Different pH values. *ACS Appl. Mater. Interfaces* **2021**, *13*, 22077-22097.
- 12. Duan, H.; Li, D.; Tang, Y.; He, Y.; Ji, S.; Wang, R.; Lv, H.; Lopes, P. P.; Paulikas, A. P.; Li, H.; Mao, S. X.; Wang, C.; Markovic, N. M.; Li, J.; Stamenkovic, V. R.; Li, Y., High-Performance Rh₂P Electrocatalyst for Efficient Water Splitting. *J. Am. Chem. Soc.* **2017**, *139*, 5494-5502.
- 13. Yang, F.; Zhao, Y.; Du, Y.; Chen, Y.; Cheng, G.; Chen, S.; Luo, W., A Monodisperse Rh₂P-Based Electrocatalyst for Highly Efficient and pH-Universal Hydrogen Evolution Reaction. *Adv. Energy Mater.* **2018**, *8*, 1703489.
- 14. Parra-Puerto, A.; Ng, K. L.; Fahy, K.; Goode, A. E.; Ryan, M. P.; Kucernak, A., Supported Transition Metal Phosphides: Activity Survey for HER, ORR, OER, and Corrosion Resistance in Acid and Alkaline Electrolytes. *ACS Catal.* **2019**, *9*, 11515-11529.
- 15. Xu, J.; Li, J.; Xiong, D.; Zhang, B.; Liu, Y.; Wu, K.-H.; Amorim, I.; Li, W.; Liu, L., Trends in activity for the oxygen evolution reaction on transition metal (M = Fe, Co, Ni) phosphide pre-catalysts. *Chem. Sci.* **2018**, *9*, 3470-3476.
- 16. Wu, X.; Wang, R.; Li, W.; Feng, B.; Hu, W., Rh₂P Nanoparticles Partially Embedded in N/P-Doped Carbon Scaffold at Ultralow Metal Loading for High Current Density Water Electrolysis. *ACS Appl. Nano Mater.* **2021**, *4*, 3369-3376.
- 17. Mutinda, S. I.; Batugedara, T. N.; Brown, B.; Adeniran, O.; Liu, Z.-F.; Brock, S. L., Rh₂P Activity at a Fraction of the Cost? Co_{2-x}Rh_xP Nanoparticles as Electrocatalysts for the Hydrogen Evolution Reaction in Acidic Media. *ACS Appl. Energy Mater.* **2021**, *4*, 946-955.
- 18. Mutinda, S. I.; Li, D.; Kay, J.; Brock, S. L., Synthesis and characterization of Co_{2-x}Rh_xP nanoparticles and their catalytic activity towards the oxygen evolution reaction. *J. Mater. Chem. A* **2018**, *6*, 12142-12152.

- 19. Liyanage, D. R.; Li, D.; Cheek, Q. B.; Baydoun, H.; Brock, S. L., Synthesis and oxygen evolution reaction (OER) catalytic performance of Ni_{2-x}Ru_xP nanocrystals: enhancing activity by dilution of the noble metal. *J. Mater. Chem. A* **2017**, *5*, 17609-17618.
- 20. Mutinda, S. I.; Batugedara, T. N.; Brown, B.; Brock, S. L., Co_{2-x}Rh_xP Nanoparticles for Overall Water Splitting in Basic Media: Activation by Phase-Segregation-Assisted Nanostructuring at the Anode. *ChemCatChem* **2021**, *13*, 4111-4119.
- 21. Du, X.; Tan, S.; Cai, P.; Luo, W.; Cheng, G., A RhNiP/rGO hybrid for efficient catalytic hydrogen generation from an alkaline solution of hydrazine. *J. Mater. Chem. A* **2016**, *4*, 14572-14576.
- 22. Muthuswamy, E.; Savithra, G. H. L.; Brock, S. L., Synthetic Levers Enabling Independent Control of Phase, Size, and Morphology in Nickel Phosphide Nanoparticles. *ACS Nano* **2011**, *5*, 2402-2411.
- 23. Henkes, A. E.; Vasquez, Y.; Schaak, R. E., Converting Metals into Phosphides: A General Strategy for the Synthesis of Metal Phosphide Nanocrystals. *J. Am. Chem. Soc.* **2007**, *129*, 1896-1897.
- 24. Jain, A. a. O., Shyue Ping and Hautier, Geoffroy and Chen, Wei and Richards, William Davidson and Dacek, Stephen and Cholia, Shreyas and Gunter, Dan and Skinner, David and Ceder, Gerbrand and Persson, Kristin a., The Materials Project: A materials genome approach to accelerating materials innovation. *APL Mater.* **2013**, *1*, 011002.
- 25. Hettiarachchi, M. A.; Su'a, T.; Abdelhamid, E.; Pokhrel, S.; Nadgorny, B.; Brock, S. L., Synthesis of colloidal MnAs_xSb_{1-x} nanoparticles: compositional inhomogeneity and magnetic consequences. *J. Mater. Chem. C* **2021**, *9*, 13292-13303.
- 26. Ha, D.-H.; Moreau, L. M.; Bealing, C. R.; Zhang, H.; Hennig, R. G.; Robinson, R. D., The Structural Evolution and Diffusion During the Chemical Transformation from Cobalt to Cobalt Phosphide Nanoparticles. *J. Mater. Chem.* **2011**, *21*, 11498-11510.
- 27. Su, L.; Cui, X.; He, T.; Zeng, L.; Tian, H.; Song, Y.; Qi, K.; Xia, B. Y., Surface reconstruction of cobalt phosphide nanosheets by electrochemical activation for enhanced hydrogen evolution in alkaline solution. *Chem. Sci.* **2019**, *10*, 2019-2024.
- 28. Xu, K.; Ding, H.; Zhang, M.; Chen, M.; Hao, Z.; Zhang, L.; Wu, C.; Xie, Y., Regulating Water-Reduction Kinetics in Cobalt Phosphide for Enhancing HER Catalytic Activity in Alkaline Solution. *Adv. Mater.* **2017**, *29*, 1606980.
- 29. Shifa, T. A.; Yusupov, K.; Solomon, G.; Gradone, A.; Mazzaro, R.; Cattaruzza, E.; Vomiero, A., In Situ-Generated Oxide in Sn-Doped Nickel Phosphide Enables Ultrafast Oxygen Evolution. *ACS Catal.* **2021**, *11*, 4520-4529.
- 30. Kim, D.; Park, S.; Yan, B.; Hong, H.; Cho, Y.; Kang, J.; Qin, X.; Yoo, T.; Piao, Y., Synthesis of Remarkably Thin Co–Fe Phosphide/Carbon Nanosheet for Enhanced Oxygen Evolution Reaction Electrocatalysis Driven by Readily Generated Active Oxyhydroxide. *ACS Appl. Energy Mater.* **2022**, *5*, 2400-2411.
- 31. Dutta, A.; Pradhan, N., Developments of Metal Phosphides as Efficient OER Precatalysts. *J. Phys. Chem. C* **2017**, *8*, 144-152.
- 32. Stern, L.-A.; Feng, L.; Song, F.; Hu, X., Ni₂P as a Janus catalyst for water splitting: the oxygen evolution activity of Ni₂P nanoparticles. *Energy Environ. Sci.* **2015**, *8*, 2347-2351.
- 33. Liu, G.; Li, P.; Zhao, G.; Wang, X.; Kong, J.; Liu, H.; Zhang, H.; Chang, K.; Meng, X.; Kako, T.; Ye, J., Promoting Active Species Generation by Plasmon-Induced Hot-Electron Excitation for Efficient Electrocatalytic Oxygen Evolution. *J. Am. Chem. Soc.* **2016**, *138*, 9128-9136.

- 34. Shinagawa, T.; Garcia-Esparza, A. T.; Takanabe, K., Insight on Tafel slopes from a microkinetic analysis of aqueous electrocatalysis for energy conversion. *Sci. Rep.* **2015**, *5*, 13801.
- 35. Wei, C.; Xu, Z. J., The Comprehensive Understanding of as an Evaluation Parameter for Electrochemical Water Splitting. *Small Methods* **2018**, *2*, 1800168.
- 36. Wei, C.; Sun, S.; Mandler, D.; Wang, X.; Qiao, S. Z.; Xu, Z. J., Approaches for measuring the surface areas of metal oxide electrocatalysts for determining their intrinsic electrocatalytic activity. *Chem. Soc. Rev.* **2019**, *48*, 2518-2534.
- 37. Stoerzinger, K. A.; Risch, M.; Han, B.; Shao-Horn, Y., Recent Insights into Manganese Oxides in Catalyzing Oxygen Reduction Kinetics. *ACS Catal.* **2015**, *5*, 6021-6031.
- 38. Sheng, W.; Myint, M.; Chen, J. G.; Yan, Y., Correlating the hydrogen evolution reaction activity in alkaline electrolytes with the hydrogen binding energy on monometallic surfaces. *Energy Environ. Sci.* **2013**, *6*, 1509-1512.
- 39. Scholz, J.; Risch, M.; Stoerzinger, K. A.; Wartner, G.; Shao-Horn, Y.; Jooss, C., Rotating Ring–Disk Electrode Study of Oxygen Evolution at a Perovskite Surface: Correlating Activity to Manganese Concentration. *J. Phys. Chem. C* **2016**, *120*, 27746-27756.
- 40. McCrory, C. C. L.; Jung, S.; Peters, J. C.; Jaramillo, T. F., Benchmarking Heterogeneous Electrocatalysts for the Oxygen Evolution Reaction. *J. Am. Chem. Soc.* **2013**, *135*, 16977-16987.
- 41. Poux, T.; Napolskiy, F. S.; Dintzer, T.; Kéranguéven, G.; Istomin, S. Y.; Tsirlina, G. A.; Antipov, E. V.; Savinova, E. R., Dual role of carbon in the catalytic layers of perovskite/carbon composites for the electrocatalytic oxygen reduction reaction. *Catal. Today* **2012**, *189*, 83-92.
- 42. Fabbri, E.; Mohamed, R.; Levecque, P.; Conrad, O.; Kötz, R.; Schmidt, T. J., Composite Electrode Boosts the Activity of Ba_{0.5}Sr_{0.5}Co_{0.8}Fe_{0.2}O_{3-δ} Perovskite and Carbon toward Oxygen Reduction in Alkaline Media. *ACS Catal.* **2014**, *4*, 1061-1070.
- 43. Yoon, Y.; Yan, B.; Surendranath, Y., Suppressing Ion Transfer Enables Versatile Measurements of Electrochemical Surface Area for Intrinsic Activity Comparisons. *J. Am. Chem. Soc.* **2018**, *140*, 2397-2400.
- 44. Surendranath, Y.; Kanan, M. W.; Nocera, D. G., Mechanistic Studies of the Oxygen Evolution Reaction by a Cobalt-Phosphate Catalyst at Neutral pH. *J. Am. Chem. Soc.* **2010**, *132*, 16501-16509.
- 45. Danilovic, N.; Subbaraman, R.; Strmcnik, D.; Chang, K. C.; Paulikas, A. P.; Stamenkovic, V. R.; Markovic, N. M., Enhancing the alkaline hydrogen evolution reaction activity through the bifunctionality of Ni(OH)₂/metal catalysts. *Angew. Chem. Int. Ed. Eng.* **2012**, *51*, 12495-8.
- 46. Malaman, B.; Le Caër, G.; Delcroix, P.; Fruchart, D.; Bacmann, M.; Fruchart, R., Magneto-elastic Transition and Magnetic Couplings: A 57Mossbauer Spectroscopy Study of the MnFeP_{1-x}As_x System. *J. Phys.: Cond. Matter* **1996**, *8*, 8653-8667.
- 47. NIST X-ray Photoelectron Spectroscopy Database, NIST Standard Reference Database Number 20, National Institute of Standards and Technology, Gaithersburg MD, 20899 (2000), doi:10.18434/T4T88K, (retrieved [4-1-2022]).
- 48. Zhang, F.-S.; Wang, J.-W.; Luo, J.; Liu, R.-R.; Zhang, Z.-M.; He, C.-T.; Lu, T.-B., Extraction of nickel from NiFe-LDH into Ni₂P@NiFe hydroxide as a bifunctional electrocatalyst for efficient overall water splitting. *Chem. Sci.* **2018**, *9*, 1375-1384.

- 49. Liu, H.; Zhu, S.; Cui, Z.; Li, Z.; Wu, S.; Liang, Y., Ni₂P nanoflakes for the high-performing urea oxidation reaction: linking active sites to a UOR mechanism. *Nanoscale* **2021**, *13*, 1759-1769.
- 50. Liyanage, D. R.; Danforth, S. J.; Liu, Y.; Bussell, M. E.; Brock, S. L., Simultaneous Control of Composition, Size, and Morphology in Discrete Ni_{2-x}Co_xP Nanoparticles. *Chem. Mater.* **2015**, *27*, 4349-4357.
- 51. Pu, Z.; Xue, Y.; Li, W.; Amiinu, I. S.; Mu, S., Efficient water splitting catalyzed by flexible NiP₂ nanosheet array electrodes under both neutral and alkaline solutions. *New J. Chem.* **2017**, *41*, 2154-2159.
- 52. Milliron, D. J.; Hughes, S. M.; Cui, Y.; Manna, L.; Li, J.; Wang, L.-W.; Alivisatos, A. P., Colloidal Nanocrystal Heterostructures with Linear and Branched Topology. *Nature Mater.* **2004**, *430*, 190-195.
- 53. Benkoula, S.; Sublemontier, O.; Patanen, M.; Nicolas, C.; Sirotti, F.; Naitabdi, A.; Gaie-Levrel, F.; Antonsson, E.; Aureau, D.; Ouf, F.-X.; Wada, S.-I.; Etcheberry, A.; Ueda, K.; Miron, C., Water adsorption on TiO₂ surfaces probed by soft X-ray spectroscopies: bulk materials vs. isolated nanoparticles. *Sci. Rep.* **2015**, *5*, 15088.
- 54. Ganesan, P.; Sivanantham, A.; Shanmugam, S., Inexpensive electrochemical synthesis of nickel iron sulphides on nickel foam: super active and ultra-durable electrocatalysts for alkaline electrolyte membrane water electrolysis. *J. Mater. Chem. A* **2016**, *4*, 16394-16402.
- 55. Liu, S.-Q.; Wen, H.-R.; Ying, G.; Zhu, Y.-W.; Fu, X.-Z.; Sun, R.; Wong, C.-P., Amorphous Ni(OH)₂ encounter with crystalline CuS in hollow spheres: A mesoporous nanoshelled heterostructure for hydrogen evolution electrocatalysis. *Nano Energy* **2018**, *44*, 7-14.
- 56. Zhang, Y.; Liao, Y.; Shi, G.; Wang, W.; Su, B., Preparation, characterization, and catalytic performance of Pd–Ni/AC bimetallic nano-catalysts. *Green Process. Syn.* **2020**, *9*, 760-769.
- 57. Kibis, L. S.; Stadnichenko, A. I.; Koscheev, S. V.; Zaikovskii, V. I.; Boronin, A. I., XPS Study of Nanostructured Rhodium Oxide Film Comprising Rh⁴⁺ Species. *J. Phys. Chem. C* **2016**, *120*, 19142-19150.
- 58. van der Walt, C.; Terblans, J. J.; Swart, H. C., A study of diffusion, atom migration and segregation in Cu and Ag alloy bulk- and nanocrystals. *AIP Adv.* **2017,** 7, 055102.
- 59. Zhang, Y.; Gao, L.; Hensen, E. J. M.; Hofmann, J. P., Evaluating the Stability of Co2P Electrocatalysts in the Hydrogen Evolution Reaction for Both Acidic and Alkaline Electrolytes. *ACS Energy Lett.* **2018**, *3*, 1360-1365.
- 60. Costa, J. D.; Lado, J. L.; Carbó-Argibay, E.; Paz, E.; Gallo, J.; Cerqueira, M. F.; Rodríguez-Abreu, C.; Kovnir, K.; Kolen'ko, Y. V., Electrocatalytic Performance and Stability of Nanostructured Fe–Ni Pyrite-Type Diphosphide Catalyst Supported on Carbon Paper. *J. Phys. Chem. C* **2016**, *120*, 16537-16544.
- 61. Liang, B.; Hu, X.; Sun, D.; Yang, Q.; Tang, H.; Zuo, X.; Lin, Y.; Li, G., Facile fabrication of bimetallic Fe₂P–Ni₂P heterostructure for boosted oxygen evolution. *J. Mater. Sci.: Mater. Electron.* **2021**, *32*, 23420-23428.
- 62. Fu, Q.; Wang, X.; Han, J.; Zhong, J.; Zhang, T.; Yao, T.; Xu, C.; Gao, T.; Xi, S.; Liang, C.; Xu, L.; Xu, P.; Song, B., Phase-Junction Electrocatalysts towards Enhanced Hydrogen Evolution Reaction in Alkaline Media. *Angew. Chem. Int. Ed.* **2021**, *60*, 259-267.

TOC

